

## Article

# The Influence of a Pumping Chamber on Hydraulic Losses in a Mixed-Flow Pump

Huiyan Zhang <sup>1,2</sup>, Fan Meng <sup>1,\*</sup>, Lei Cao <sup>1</sup>, Yanjun Li <sup>1,3</sup> and Xinkun Wang <sup>1</sup>

<sup>1</sup> Research Center of Fluid Machinery Engineering and Technology, Jiangsu University, Zhenjiang 212013, China; zhy@hytc.edu.cn (H.Z.); cl007755@163.com (L.C.); lyj782900@ujs.edu.cn (Y.L.); xjwxk@126.com (X.W.)

<sup>2</sup> School of Computer Science and Technology, Huaiyin Normal University, Huai'an 223300, China

<sup>3</sup> Institute of Fluid Engineering Equipment, JITRI, Zhenjiang 212009, China

\* Correspondence: mf@ujs.edu.cn

**Abstract:** In this study, entropy generation theory based on computational fluid dynamics (CFD) is used to study the influence of a pumping chamber type (guide vane and volute scheme) on the spatial distribution of hydraulic loss in a mixed-flow pump. The CFD data of the mixed-flow pump with a volute is validated by external characteristic test data under  $Q = 561.4\text{--}1598.6\text{ m}^3/\text{h}$ . The results show that the efficiency and the head of the guide vanes scheme are lower under  $Q = 800\text{--}1200\text{ m}^3/\text{h}$ , which resulted from a higher total entropy production (TEP) in the pumping chamber and outlet pipe. The high total entropy production rate (TEPR) inside the guide vanes can be found near the leading edge of the hub side and trailing edge of the rim side due to flow separation, which reduces the recovery efficiency of kinetic energy of the guide vanes. The high TEPR inside outlet pipe can be seen near the inlet, caused by back flow. However, the efficiency and head of the volute scheme are lower, under  $Q = 1200\text{--}1600\text{ m}^3/\text{h}$ , owing to the fact that the volute cannot effectively convert kinetic energy into pressure energy and thus the high TEPR can be found near outlet of volute and inlet of outlet pipe. These results can provide useful suggestions to the matching optimization of the impeller and pumping chamber in a mixed-flow pump.

**Keywords:** mixed-flow pump; pumping chamber; volute; guide vanes; entropy production



**Citation:** Zhang, H.; Meng, F.; Cao, L.; Li, Y.; Wang, X. The Influence of a Pumping Chamber on Hydraulic Losses in a Mixed-Flow Pump. *Processes* **2022**, *10*, 407. <https://doi.org/10.3390/pr10020407>

Academic Editors: Jin-Hyuk Kim, Wenjie Wang, Giorgio Pavesi, Lijian Shi and Ji Pei

Received: 30 January 2022

Accepted: 16 February 2022

Published: 19 February 2022

**Publisher's Note:** MDPI stays neutral with regard to jurisdictional claims in published maps and institutional affiliations.



**Copyright:** © 2022 by the authors. Licensee MDPI, Basel, Switzerland. This article is an open access article distributed under the terms and conditions of the Creative Commons Attribution (CC BY) license (<https://creativecommons.org/licenses/by/4.0/>).

## 1. Introduction

The mixed-flow pump has the advantages of a large flow rate, a widely applicable head variation range, a broad efficient operation area, and difficult cavitation, and they are widely used in agricultural irrigation, urban water supply, and regional water transfer. A mixed-flow pump is divided into mixed-flow pumps with guide vanes and mixed-flow pumps with a volute according to the pumping chamber form [1]. Compared with a mixed-flow pump with guide vanes, a mixed-flow pump with a volute has a shorter axial size and rotation shaft length, resulting in a simple operation and sustainable operations in harsh environments [2]. However, the hydraulic design theory of traditional mixed-flow pump impeller was based on guide vanes, and thus the matching optimization of the impeller and volute lacks corresponding theoretical basis. The recovery efficiency of kinetic energy inside the impeller outflow is the key to determine the matching between pumping chamber and impeller. Therefore, the local high hydraulic losses in the mixed-flow pump with a volute and guide vanes should be compared and analyzed.

With the rapid development of computer technology, computational fluid dynamics (CFD) can produce a more in-depth flow, material and energy transfer analysis of the internal flow field of pumps [3], and the calculated results can provide an important reference for engineers [4,5]. Therefore, numerical simulations based on CFD have become the main research method for mixed-flow pumps. For example, Liu [6] and Han [7] numerically studied the tip leakage flow characteristics in a mixed-flow pump as a turbine,

which provides a reference for the design of the tip clearance size. Li [8], Xu [9], and Ji [10] numerically predicted the distribution characteristics of external characteristic parameters and the internal flow fields of mixed flow pumps under a startup transition process, off-design condition, and a saddle zone, respectively. The calculated results have important engineering value for the safe operation of mixed flow pumps under unstable conditions. In addition, Kim [11,12] optimized the axial projection shape of a mixed flow pump impeller based on CFD technology, which significantly improved the cavitation performance and hydraulic performance of the mixed flow pump.

However, the literature on mixed-flow pumps mainly focuses on the analysis of internal pressure fields and velocity fields, and there is little research on the mechanisms of internal energy loss and energy transfer. Due to the continuous development of entropy generation theory, based on the second law of thermodynamics, more and more scholars have analyzed the spatial distribution characteristics of energy losses inside fluid machinery by using entropy generation as an evaluation index of energy loss. Bejan [13] found that the increase in entropy production in fluid motion was mainly due to the decrease in available energy, and first proposed the concept of minimizing entropy production. Spurk et al. [14] proposed an entropy balance equation for incompressible fluids. Herwig [15,16] and Kock et al. [17,18] used time-averaged equations and divided entropy production into four categories that led to entropy production and can be obtained through CFD post-processing. Hou [19] used range analysis based on entropy production to optimize a centrifugal pump. The area of high hydraulic loss inside the volute was significantly reduced after optimization. Guan [20] applied entropy production theory to analyze the internal hydraulic loss characteristics of a double-suction centrifugal pump under different flow rates. The results show that the location of high hydraulic loss in the volute shifted from inlet to the baffle and tongue with the increase in flow rate. Yang [21] studied the distribution of entropy rate in guide vanes of an axial flow pump under different flow rates. He found that the area of high hydraulic losses decreased with increase in flow rate, but it increased with the shortening of the axial distance from the outlet. In summary, the entropy generation theory based on CFD can visualize the internal energy loss of guide vanes and the volute, and provide a more intuitive reference for optimal designs. However, there is little public literature that uses entropy production theory to study the recovery efficiency of rotating kinetic energy in the pumping chamber of a mixed-flow pump. The relationship between the type of pumping chamber and the spatial distribution of hydraulic losses inside the mixed flow pump cannot be established. The lack of pumping chamber type's influence on high hydraulic loss limits the development of matching design between impeller and different pumping chambers.

In this study, a combination of simulation and experiment is used to deeply analyze the internal flow characteristics of guide vane mixed-flow pump and volute mixed-flow pump with the same impeller model, and compares the changes caused by different pressure chamber forms. Based on entropy generation theory, the hydraulic losses of the two mixed-flow pumps are calculated and the location of high hydraulic losses is obtained. The different flow loss mechanisms in the mixed-flow pump with guide vanes and a volute are explored.

## 2. Numerical Simulation Method

### 2.1. Three-Dimensional Geometry Model

In this study, the rotation speed of a mixed-flow pump with guide vanes and a volute were both 1450 r/min. The main parameters of the two mixed-flow pumps with the same impeller model were as follows: impeller diameter was  $D = 320$  mm and number of blades was  $Z_1 = 3$ . Creo software was used to complete the three-dimensional modeling of the two mixed-flow pump models, as shown in Figure 1.

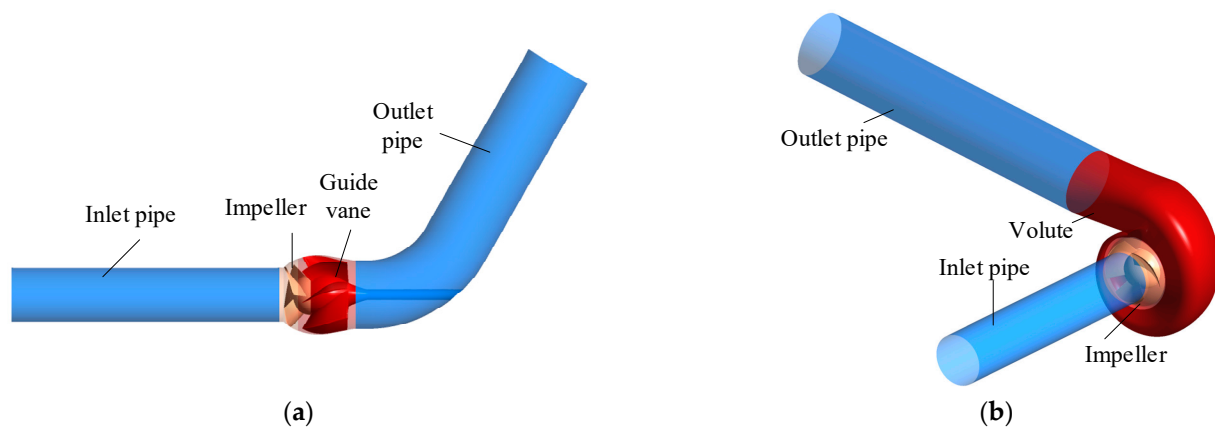


**Figure 1.** A 3D schematic diagram of (a) mixed-flow pump with guide vanes and (b) mixed-flow pump with a volute.

The best efficiency point of the mixed-flow pump with guide vanes was  $Q_{d1} = 1400 \text{ m}^3/\text{h}$  and the specific speed was  $n_{s1} = 593.5$ . The number of guide vanes was  $Z_2 = 7$ ; the best efficiency point of the volute mixed-flow pump was  $Q_{d2} = 1200 \text{ m}^3/\text{h}$ , and the specific speed was  $n_{s2} = 593.0$ . The formula of pump performance parameters is as follows:

$$H = \frac{p_{\text{out}} - p_{\text{in}}}{\rho g} \quad (1)$$

$$\eta = \frac{\rho g H Q}{3600 P_s} \quad (2)$$

$$n_s = \frac{3.65 n Q_d^{0.5}}{H_d^{0.75}} \quad (3)$$

where  $H$ ,  $\rho$  and  $g$  stand for head, water density and gravitational acceleration, respectively.  $p_{\text{out}}$  and  $p_{\text{in}}$  are the total pressure of inlet and outlet.  $\eta$ ,  $Q$  and  $P_s$  are the pump efficiency, volume flow rate and shaft power.  $n$  and  $Q_d$  represent for the rotation speed and volume flow rate of best efficiency;  $H_d$  stands for the head under best efficiency point.

## 2.2. Mesh Generation

The grids were divided into structured grids and unstructured grids, according to the shape and storage data structure. Compared with unstructured grids, structured grids take up fewer computing resources and have a faster convergence rate. Structural meshing is a time-consuming and vital step in the pre-processing of numerical simulations. Reasonable meshing can ensure a higher calculation accuracy and better convergence of CFD. Therefore, this paper uses ICEM to divide the inlet and outlet channels and the volute parts of the two mixed-flow pumps into a structured grid. The TurboGrid was used to generate a structural grid of the guide vanes. The details of the grid are shown in Figure 2. In addition, the distribution of dimensionless coefficient  $Y_+$  on walls is shown in Figure 3. The mean  $Y_+$  of the impeller was 33.24, the average value of the guide vanes was 23.21, and the average value of the volute was 43.03, indicating that the near-wall surface in this work can meet the mesh size requirements of the selected turbulence model, and can better reflect flow field characteristics at the near-wall surface.

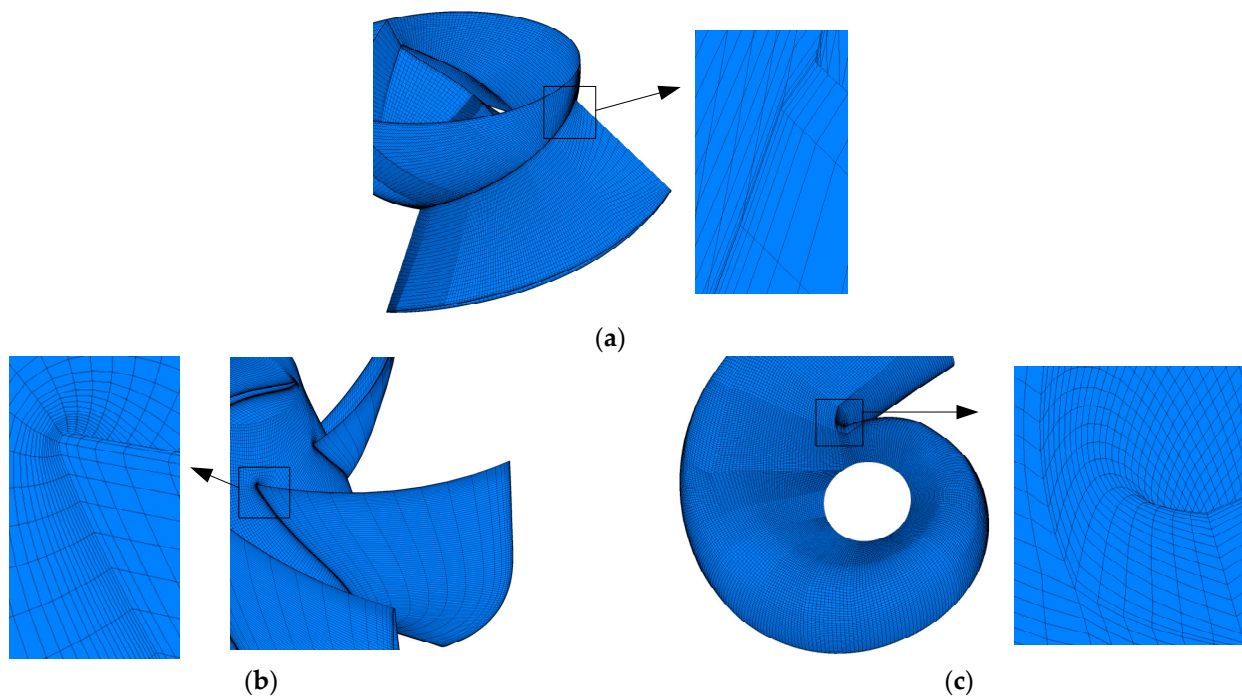


**Figure 2.** Schematic diagram of the detailed grid of the (a) impeller blade, (b) guide vanes, and (c) volute.

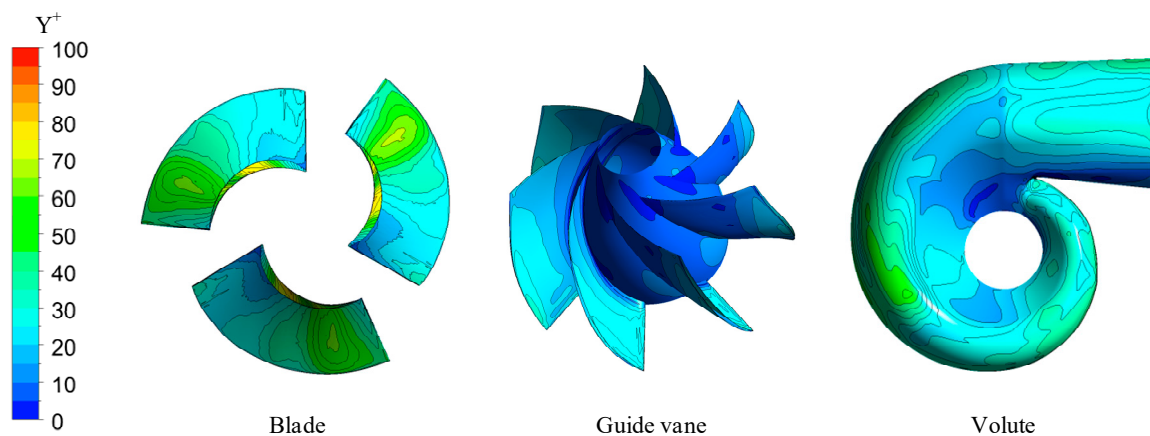


**Figure 3.**  $Y^+$  value of each component.

### 2.3. Conservation Equations and Boundary Conditions

In this paper, the unsteady Reynolds time-average equation was used as the governing equation, and the SST  $k-\omega$  turbulence model was applied to enclose the governing equation. The boundary condition settings of the two mixed-flow pumps were the same: the working medium was water at 25 °C, the inlet boundary condition was set to mass flow, the outlet boundary condition was set to static pressure, and the reference pressure was 1 standard atmosphere; the impeller was set to the rotating domain. The inlet pipe, outlet pipe, volute, and guide vanes were all set as static domains. In addition, the results of the steady calculation were used as the initial condition for unsteady calculation. The interface between rotor and stator of the steady calculation was set to ‘Frozen Rotor’; the grid connection mode was selected as GGI, and the convergence residual value was set to  $10^{-4}$ . The interface between rotor and stator of the unsteady calculation was ‘Transient Rotor Stator’, and the convergence residual value was  $10^{-5}$ . The time step was 0.00034483 s and the total time was 0.537931 s.

#### 2.4. Entropy Production Theory

The transport equation of entropy production is based on the second law of thermodynamics, and the calculation formula is as follows [15–18]:

$$\rho \left( \frac{\partial s}{\partial t} + u \frac{\partial s}{\partial x} + v \frac{\partial s}{\partial y} + w \frac{\partial s}{\partial z} \right) = \text{div} \left( \frac{\vec{q}}{T} \right) + \frac{\Phi}{T} + \frac{\Phi_{\theta}}{T^2} \quad (4)$$

where  $s$  is specific entropy.  $u$ ,  $v$  and  $w$  represent the velocity components in the  $x$ ,  $y$ , and  $z$  directions of Cartesian coordinates, respectively.  $T$  is the thermodynamic temperature.  $\text{div} \left( \frac{\vec{q}}{T} \right)$  indicates the reversible heat transfer.  $\frac{\Phi}{T}$  is the entropy production due to dissipation increase and  $\frac{\Phi_{\theta}}{T^2}$  is the entropy production caused by the heat transfer.

Since the working medium inside the mixed-flow pump was set as constant temperature incompressible fluid [20,21],  $\frac{\Phi}{T}$  is the only source of entropy production inside the mixed-flow pump. In addition, the computational domain control equation is the Reynolds time-average equation, and hence the calculation formula of  $\frac{\Phi}{T}$  after time-averaged is as follows:

$$\overline{\left( \frac{\Phi}{T} \right)} = \frac{(\Phi_D + \Phi_I)}{\bar{T}} \quad (5)$$

$$\frac{\Phi_D}{\bar{T}} = \frac{\mu}{\bar{T}} \left\{ 2 \left[ \left( \frac{\partial \bar{u}}{\partial x} \right)^2 + \left( \frac{\partial \bar{v}}{\partial y} \right)^2 + \left( \frac{\partial \bar{w}}{\partial z} \right)^2 \right] + \left( \frac{\partial \bar{u}}{\partial y} + \frac{\partial \bar{v}}{\partial x} \right)^2 + \left( \frac{\partial \bar{v}}{\partial z} + \frac{\partial \bar{w}}{\partial y} \right)^2 + \left( \frac{\partial \bar{u}}{\partial z} + \frac{\partial \bar{w}}{\partial x} \right)^2 \right\} \quad (6)$$

$$\frac{\Phi_I}{\bar{T}} = \frac{\mu}{\bar{T}} \left\{ 2 \left[ \overline{\left( \frac{\partial u'}{\partial x} \right)^2} + \overline{\left( \frac{\partial v'}{\partial y} \right)^2} + \overline{\left( \frac{\partial w'}{\partial z} \right)^2} \right] + \overline{\left( \frac{\partial u'}{\partial y} + \frac{\partial v'}{\partial x} \right)^2} + \overline{\left( \frac{\partial v'}{\partial z} + \frac{\partial w'}{\partial y} \right)^2} + \overline{\left( \frac{\partial u'}{\partial z} + \frac{\partial w'}{\partial x} \right)^2} \right\} \quad (7)$$

where  $\frac{\Phi_D}{\bar{T}}$  and  $\frac{\Phi_I}{\bar{T}}$  are the direct entropy production rate (DEPR) and indirect entropy production rate (IEPR).  $\bar{u}$ ,  $\bar{v}$  and  $\bar{w}$  represent the time-averaged velocity components in the  $x$ ,  $y$ , and  $z$  directions of Cartesian coordinates, respectively.  $u'$ ,  $v'$  and  $w'$  represent the velocity fluctuation components in the  $x$ ,  $y$ , and  $z$  directions of Cartesian coordinates, respectively, respectively.  $\mu$  is the dynamic viscosity.

The velocity fluctuation cannot be obtained by solving the Reynolds time-average equation; therefore, Knock [17,18] proposed Equation (8), so that IEPR  $\frac{\Phi_I}{\bar{T}}$  can be obtained in CFD post-processing.

$$\frac{\Phi_I}{\bar{T}} = \frac{\rho \varepsilon}{\bar{T}} \quad (8)$$

where  $\varepsilon$  is the turbulent dissipation rate.

In addition, total entropy production rate (TEPR)  $\frac{\Phi_T}{\bar{T}}$ , indirect entropy production (IEP)  $S_{\text{pro,I}}$ , direct entropy production (DEP)  $S_{\text{pro,D}}$ , and total entropy production (TEP)  $S_{\text{pro,T}}$  can be calculated as follows:

$$\frac{\Phi_T}{\bar{T}} = \frac{\Phi_I + \Phi_D}{\bar{T}} \quad (9)$$

$$S_{\text{pro,D}} = \int_V \frac{\Phi_D}{\bar{T}} dV \quad (10)$$

$$S_{\text{pro,I}} = \int_V \frac{\Phi_I}{\bar{T}} dV \quad (11)$$

$$S_{\text{pro,T}} = S_{\text{pro,D}} + S_{\text{pro,I}} \quad (12)$$

#### 2.5. Validation of Numerical Simulation

In order to verify the accuracy of the numerical simulations, the external characteristic tests of the mixed-flow pump with a volute were completed on a closed test bench, as shown in Figure 4. The test bench was divided into upper and lower layers. The height of

upper layer was 4.6 m and that of lower layer was  $-2.6$  m. The mixed-flow pump with a volute, motor, torque meter and differential pressure sensor were located on the upper layer. An auxiliary pump and a flow meter were located on the lower layer. The operating flow of the mixed-flow pump was controlled by electric valves. The flow rate, rotating shaft power, and head were measured using an intelligent electromagnetic flowmeter, JCL2 intelligent torque speed sensor (1–500 N·m), and EJA intelligent differential pressure transmitter (0–25 m), respectively. The measurement uncertainty of flow rate  $E_Q$ , shaft power  $E_T$ , and head  $E_H$  was less than 0.2%, 0.14% and 0.1%, respectively. The measurement uncertainty of the test bench  $E_S$  was less than 0.26% calculated by  $E_S = \sqrt{E_Q^2 + E_T^2 + E_H^2}$ , which meets the requirements of SL140-2006.



Figure 4. Test bench of a mixed-flow pump with a volute.

The calculation and test results of the external characteristics of the mixed-flow pump with a volute are shown in Figure 5. The efficiency of the volute mixed-flow pump reached its maximum value under the designed flow rate, but the efficiency dropped sharply with the increase in the flow rate. Therefore, analyzing the internal flow characteristics of the volute mixed-flow pump under a large flow rate and determining the mechanism of the sharp drop in efficiency is of great significance to broaden the operating range of volute mixed-flow pumps. In addition, the maximum relative error between the calculation and the test head was less than 1% and the maximum relative error between the calculation and test efficiency was less than 4%. The maximum relative error between the calculation value and the experimental value was less than 5%, which shows that the numerical simulation method used in this paper meets the requirements, and that the calculation results are reliable.

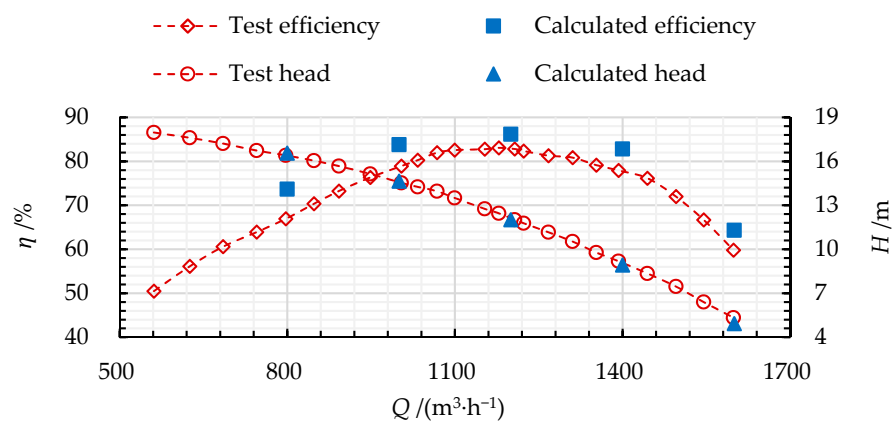
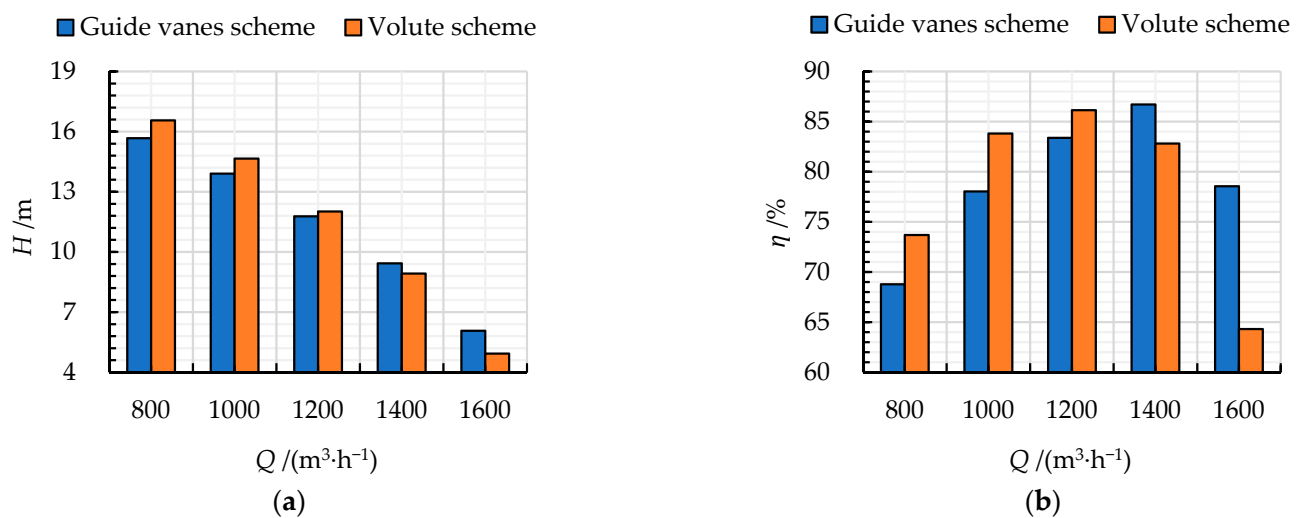


Figure 5. Comparison of test and calculated results of the mixed-flow pump with a volute.

### 3. Analysis of Calculation Results

#### 3.1. Comparison of Pump Performance

The comparison of pump performance between the mixed-flow pump with guide vanes and a volute can be shown in Figure 6. The  $H$  and  $\eta$  of the guide vanes mixed-flow pump are lower than that of the volute mixed-flow pump under  $Q = 800 - 1200 \text{ m}^3/\text{h}$ , but the  $H$  and  $\eta$  of the guide vanes mixed-flow pump are higher than that of the volute mixed-flow pump under  $Q = 1200 - 1600 \text{ m}^3/\text{h}$ . The relative deviation of  $H$  and  $\eta$  between the mixed-flow pump with guide vanes and volute both increased with the increase in flow rate under  $Q = 1000 - 1600 \text{ m}^3/\text{h}$ . The minimum relative deviation of  $H$  and  $\eta$  were  $-0.05\%$  and  $-6.89\%$ , respectively. The maximum relative deviation of  $H$  and  $\eta$  were  $0.23\%$  and  $22.14\%$ . The results illustrated that the recovery efficiency of kinetic energy of volute is slightly higher than that of the guide vanes under smaller flow rate, but the recovery efficiency of kinetic energy of the volute was significantly lower than that of the guide vanes under large flow rate. In addition, from the point of view of the mixed-flow pump with a volute, the head plays an important role. Therefore, the high local energy losses in the two types of the mixed-flow pump should be compared and analyzed to widen the high efficiency range of the volute mixed-flow pump without significantly reducing the head.



**Figure 6.** Comparison of the (a) head and (b) efficiency of the mixed-flow pump under guide vanes and volute scheme.

#### 3.2. TEP Distribution in Different Pump Components

In this study, the energy losses were evaluated by the entropy production, which was divided into IEP and DEP. The distributions of IEP and DEP of different components in the guide vanes mixed-flow pump are shown in Figure 7a,b. The IEP of the guide vanes and the impeller is much higher than that of other hydraulic components at small flow rates and the designed flow rate. The IEP of the guide vanes and outlet pipe decreases with an increase in flow rate due to the fact that the circumferential velocity decreased with the increase in flow rate. The IEP of impeller firstly decreases and then increases with an increase in flow rate, and it reaches the minimum value under  $Q = 1000 \text{ m}^3/\text{h}$ , where the impeller had the highest work efficiency. The IEP of inlet pipe increases with an increase in flow rate caused by that axial velocity increased with the flow rate increasing. In addition, the DEP is significantly lower than the IEP of each pump component. The DEP of the inlet pipe and outlet pipe is so low that it can be negligible. The DEP of the impeller increases with the increase in the flow rate, and the DEP of the guide vanes decreases first and then increases with an increase in flow rate.

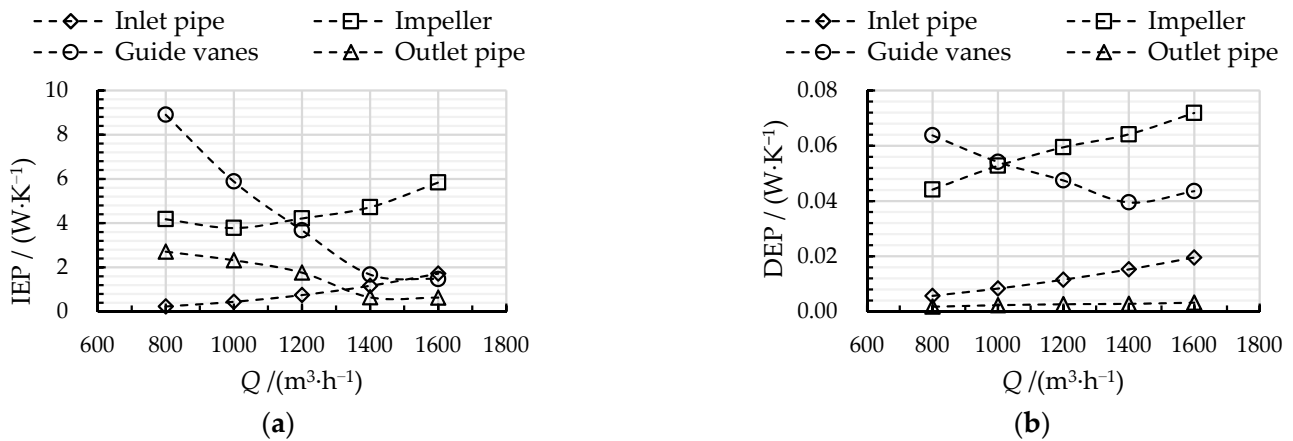


Figure 7. The distribution of (a) IEP and (b) DEP in mixed-flow pumps with guide vanes.

Figure 8 shows the distribution of IEP and DEP of different pump components in the mixed-flow pump with a volute. As shown in Figure 8a, the IEP of the impeller and volute is much higher than that of the inlet pipe and outlet pipe at small flow rates and the best efficiency point. The IEP curves of the impeller and inlet were similar to that in Figure 7a. The IEP of the impeller first declines and then rises with the increase in flow rate, and the IEP of the inlet pipe rises with the increase in flow rate. Although the circumferential velocity decreased with increasing flow rate, the recovery efficiency of kinetic energy of volute is low under large flow rates. The IEP of the volute firstly decreases sharply and then increases slightly with the increase in flow rate. The IEP of the outlet pipe increases with the increase in flow rate. As shown in Figure 8b, the DEP inside the mixed-flow pump with a volute is also significantly lower than the IEP. The IEP of the volute remain stable with an increase in flow rate, while IEP of the other hydraulic components rises with the increase in flow rate.

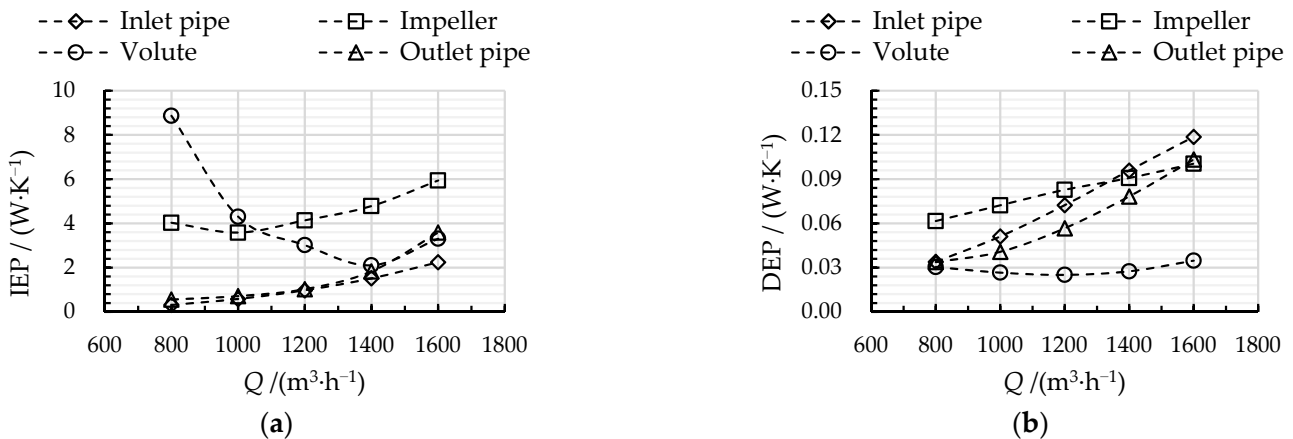
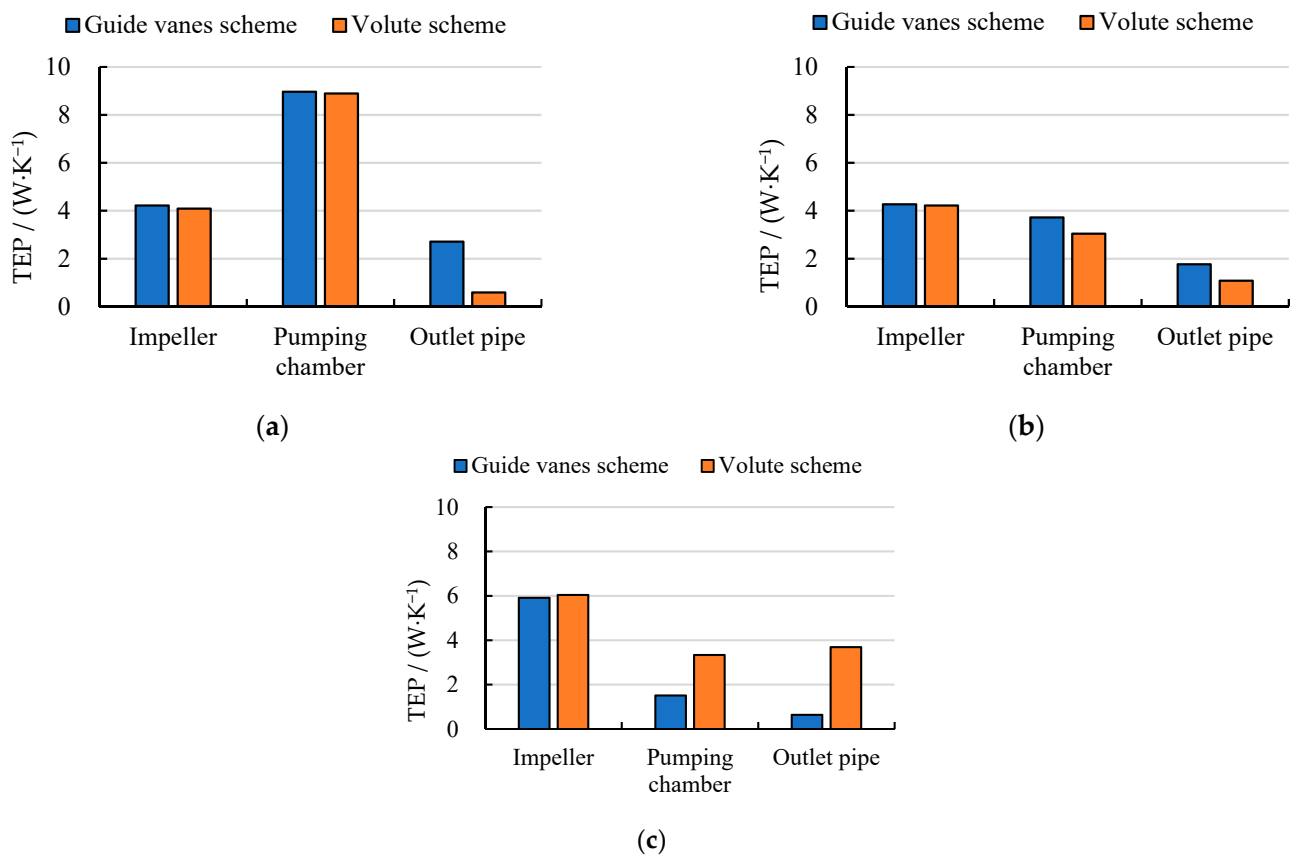


Figure 8. The distribution of (a) IEP and (b) DEP in the mixed-flow pump with a volute.

Figure 9 shows a comparison of the TEP between the mixed-flow pump with guide vanes and a volute under three flow rates. Since the inlet pipe was located upstream of the pumping chamber and impeller, the TEP of the inlet pipe was low and not affected by the type of pumping chamber. Although the impeller was also located upstream of the pumping chamber, the TEP of impeller were different in two types of mixed-flow pump due to the fact that interference effect between the impeller and pumping chamber was closely related to the type of pumping chamber. In addition, the type of pumping chamber and the operating flow rate played key roles in the TEP of the pumping chamber and outlet pipe. Under  $Q = 800 m^3/h$ , there is little difference in the TEP between the volute and the guide vanes due to the similar ability to recover rotational kinetic energy. The TEP of the impeller

and outlet pipe in the mixed-flow pump with guide vanes is higher than that with a volute. The relative deviations of the impeller and outlet pipe between the mixed-flow pump with guide vanes and a volute were 3.2% and 360.2%, respectively. Under  $Q = 1200 \text{ m}^3/\text{h}$ , the TEP of the impeller, pumping chamber and outlet pipe in the mixed-flow pump with guide vanes is higher than that with a volute. The relative deviations of impeller, pumping chamber and outlet pipe between the mixed-flow pump with guide vanes and a volute were 1.3% 22.4% and 63.0%, respectively. Under  $Q = 1600 \text{ m}^3/\text{h}$ , the TEP of the impeller, pumping chamber and outlet pipe in the mixed-flow pump with guide vanes is lower than that with a volute caused by that the guide vanes have a higher ability to recover rotating kinetic energy under large flow rates. The relative deviations of impeller, pumping chamber and outlet pipe between the mixed-flow pump with guide vanes and a volute are  $-2.2\%$   $-54.7\%$  and  $-82.7\%$ , respectively.



**Figure 9.** The comparison of TEP of pump components between guide vanes and volute scheme under (a)  $800 \text{ m}^3/\text{h}$ , (b)  $1200 \text{ m}^3/\text{h}$ , and (c)  $1600 \text{ m}^3/\text{h}$ .

### 3.3. TEP Rate Distribution of Impeller-Pumping Chamber Interface

The rotor and stator interference (RSI) between impeller and pumping chamber improve flow instability and produce additional velocity losses. Thus, the intensity of the interference caused by the type of pumping chamber plays a key role in the distribution of velocity and TEP rate. The velocity circulation at impeller outlet can represent the strength of rotational kinetic energy inside the impeller outflow. The velocity circulation  $\Gamma$  and radial coefficient  $r^*$  can be calculated as follows:

$$\Gamma = \oint_L \vec{v}_u \cdot d\vec{l} \quad (13)$$

$$r^* = \frac{r_c - r_h}{r_s - r_h} \quad (14)$$

where  $v_u$  stands for absolute circumferential velocity, and  $L$  and  $d\vec{l}$  are the length of the calculated ring and unit length, respectively.  $r_c$ ,  $r_h$  and  $r_s$  are the calculated radius, hub radius and rim radius, respectively.

The comparison of radial distribution of  $\Gamma$  at the impeller outlet between guide vanes and volute scheme was shown in Figure 10. The radial coefficient can be calculated by. When  $Q = 800 \text{ m}^3/\text{h}$ ,  $\Gamma$  rises with the increase in  $r^*$  under both guide vanes and volute schemes.  $\Gamma$  under guide vanes scheme is obviously lower than that under volute scheme within  $r^* < 0.4$ , but  $\Gamma$  under guide vanes scheme is slightly higher than that under the volute scheme under the remaining  $r^*$ . The  $\Gamma$  curves under  $Q = 1200 \text{ m}^3/\text{h}$  are similar to that under  $Q = 800 \text{ m}^3/\text{h}$ .  $\Gamma$  under guide vanes scheme is evidently lower than that under the volute scheme within  $r^* < 0.2$ . When  $Q = 1600 \text{ m}^3/\text{h}$ ,  $\Gamma$  declines firstly and then increase with the increase in  $r^*$  under both guide vanes and volute schemes. There is no evident difference in the radial distribution of  $\Gamma$  between the two schemes. Figure 11 shows the spatial distribution of TEPR at the impeller outlet due to RSI between the impeller and pumping chamber. When  $Q = 800 \text{ m}^3/\text{h}$ , the evident high TEPR can be found near the hub under both guide vanes and volute schemes. The area of high TEPR under the guide vanes scheme is larger than that under the volute scheme. When  $Q = 1200 \text{ m}^3/\text{h}$ , the area of high TEPR becomes small under two schemes, but the area of high TEPR under the guide vanes scheme is still larger than that under the volute scheme. When  $Q = 1600 \text{ m}^3/\text{h}$ , the distribution of TEPR under the guide vanes scheme is similar to that under the volute scheme, and there is no obvious high TEPR. The results shown that the RSI between impeller and guide vanes is stronger under  $Q = 800$  and  $1200 \text{ m}^3/\text{h}$ , which leads to more velocity losses and TEPR near the hub side of the impeller outlet, compared with the RSI between impeller and volute.

### 3.4. TEPR Rate Distribution of Pumping Chamber

The inflow and outflow directions of the guide vanes were parallel to the rotation axis. However, the inflow direction was parallel to the rotation axis, and the outflow direction was perpendicular to the rotation axis in the volute. Therefore, the mechanism of transforming kinetic energy into pressure energy between the guide vane and volute is different. To compare the conversion capability of kinetic energy between guide vanes and volute, the impeller outflow was divided into axial velocity and circumferential velocity, and pressure was used as the evaluation unit of kinetic energy and pressure energy in this study. The axial kinetic pressure (AKP) and circumferential kinetic pressure (CKP) can be calculated as follows:

$$\text{AKP} = 0.5\rho v_m^2 \quad (15)$$

$$\text{CKP} = 0.5\rho v_c^2 \quad (16)$$

where  $v_m$  is the average axial velocity and  $v_c$  is the average circumferential velocity.

The distributions of AKP, CKP and static pressure (SP) on the inlet and outlet of two pumping chamber under different flow rates are shown in Figure 12. In the guide vanes, the AKP and SP on the inlet is lower than that on the outlet. The relative increase ratios between the outlet and inlet of AKP were 116.2%, 84.7% and 8.4% under  $800 \text{ m}^3/\text{s}$ ,  $1200 \text{ m}^3/\text{s}$ ,  $1600 \text{ m}^3/\text{s}$ , respectively. The relative increase ratios between the outlet and inlet of SP were 0.5%, 5.1% and 4.8% under  $800 \text{ m}^3/\text{s}$ ,  $1200 \text{ m}^3/\text{s}$ ,  $1600 \text{ m}^3/\text{s}$ , respectively. However, the CKP on the inlet is significantly higher than that on the outlet. The relative decrease ratios between the outlet and inlet of CKP were 85.3%, 87.2% and 83.8% under  $800 \text{ m}^3/\text{s}$ ,  $1200 \text{ m}^3/\text{s}$ ,  $1600 \text{ m}^3/\text{s}$ , respectively. The results shown that the guide vane not only converts part of CKP into SP, but also converts part of CKP into AKP. The conversion efficiency between kinetic energy and pressure energy is the highest under design flow rate. In the volute, the AKP is higher than that on the outlet and the relative decrease ratios between the outlet and inlet were 98.3%, 95.9% and 97.4% under  $800 \text{ m}^3/\text{s}$ ,  $1200 \text{ m}^3/\text{s}$ ,  $1600 \text{ m}^3/\text{s}$ , respectively. The CKP and SP on the inlet are higher and lower, respectively than that on the outlet, under  $Q \leq 1200 \text{ m}^3/\text{s}$ . The relative decrease ratios of CKP between the outlet

and inlet were 97.1% and 83.0% under  $800 \text{ m}^3/\text{s}$  and  $1200 \text{ m}^3/\text{s}$ . The relative increase ratios of SP between the outlet and inlet were 30.2% and 15.6% under  $800 \text{ m}^3/\text{s}$  and  $1200 \text{ m}^3/\text{s}$ . However, the CKP and SP on the inlet are lower and higher, respectively than that on the outlet, under  $Q = 1600 \text{ m}^3/\text{s}$ . The results explained that all almost kinetic pressure was converted into static pressure and energy dissipation under  $800 \text{ m}^3/\text{s}$  and  $1200 \text{ m}^3/\text{s}$ , which results in low kinetic pressure inside the volute outflow. However, the volute cannot effectively convert kinetic pressure into SP.

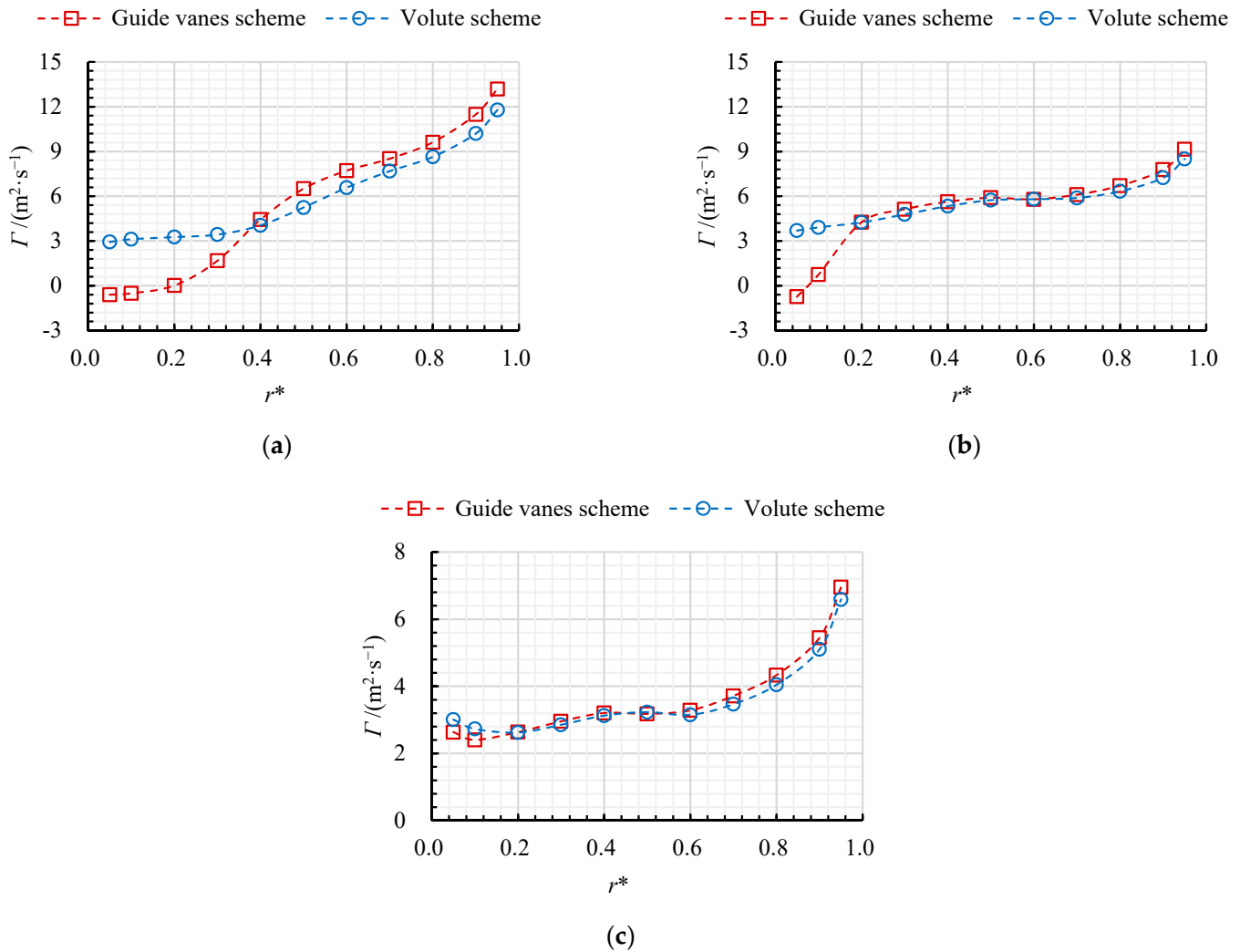


**Figure 10.** The average radial distribution of  $\Gamma$  at impeller outlet under (a)  $Q = 800 \text{ m}^3/\text{h}$ , (b)  $Q = 1200 \text{ m}^3/\text{h}$ , and (c)  $Q = 1600 \text{ m}^3/\text{h}$ .

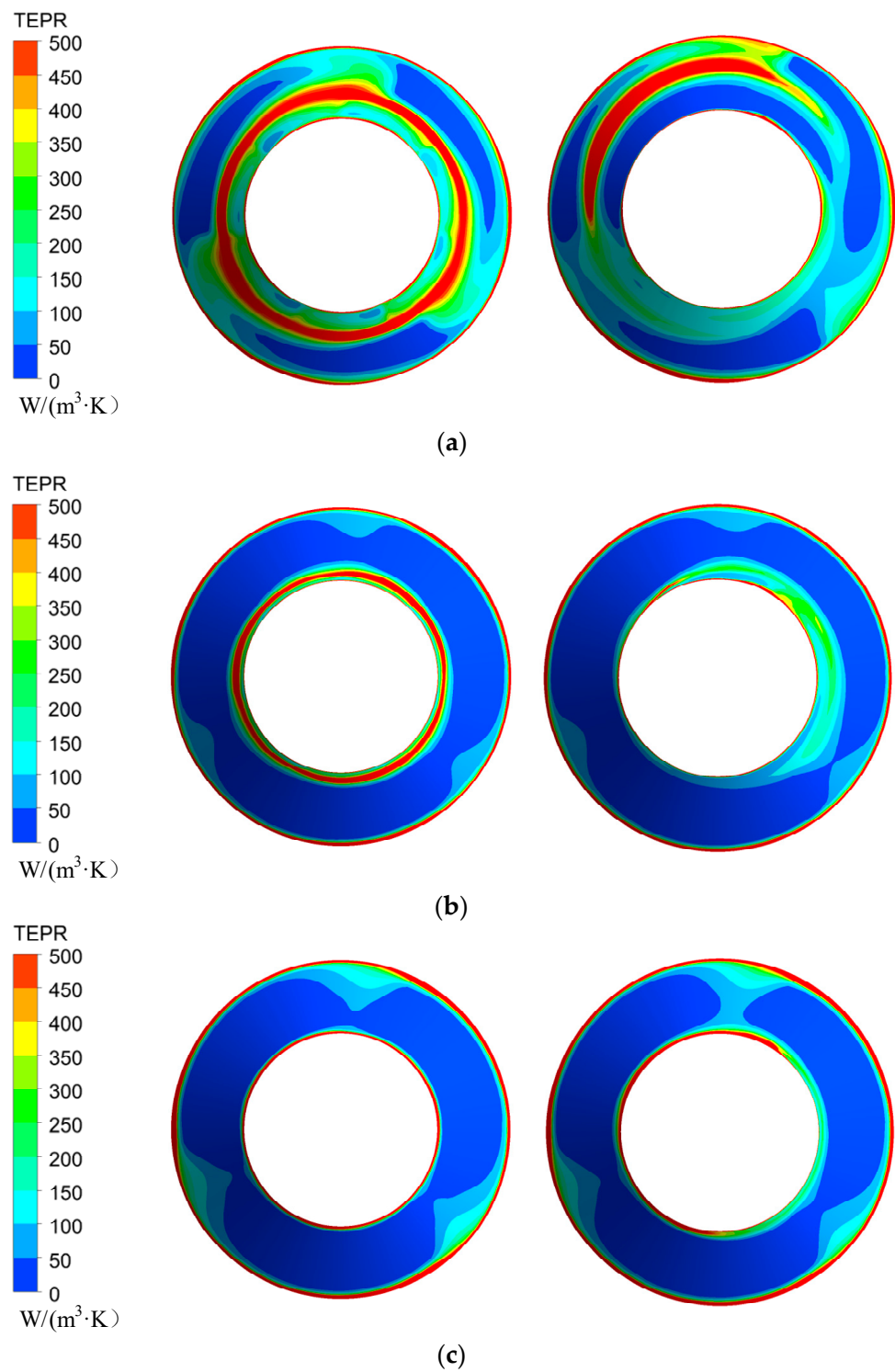


**Figure 11.** The distributions of TEPR at impeller outlet under (a)  $Q = 800 \text{ m}^3/\text{h}$ , (b)  $Q = 1200 \text{ m}^3/\text{h}$ , and (c)  $Q = 1600 \text{ m}^3/\text{h}$ .

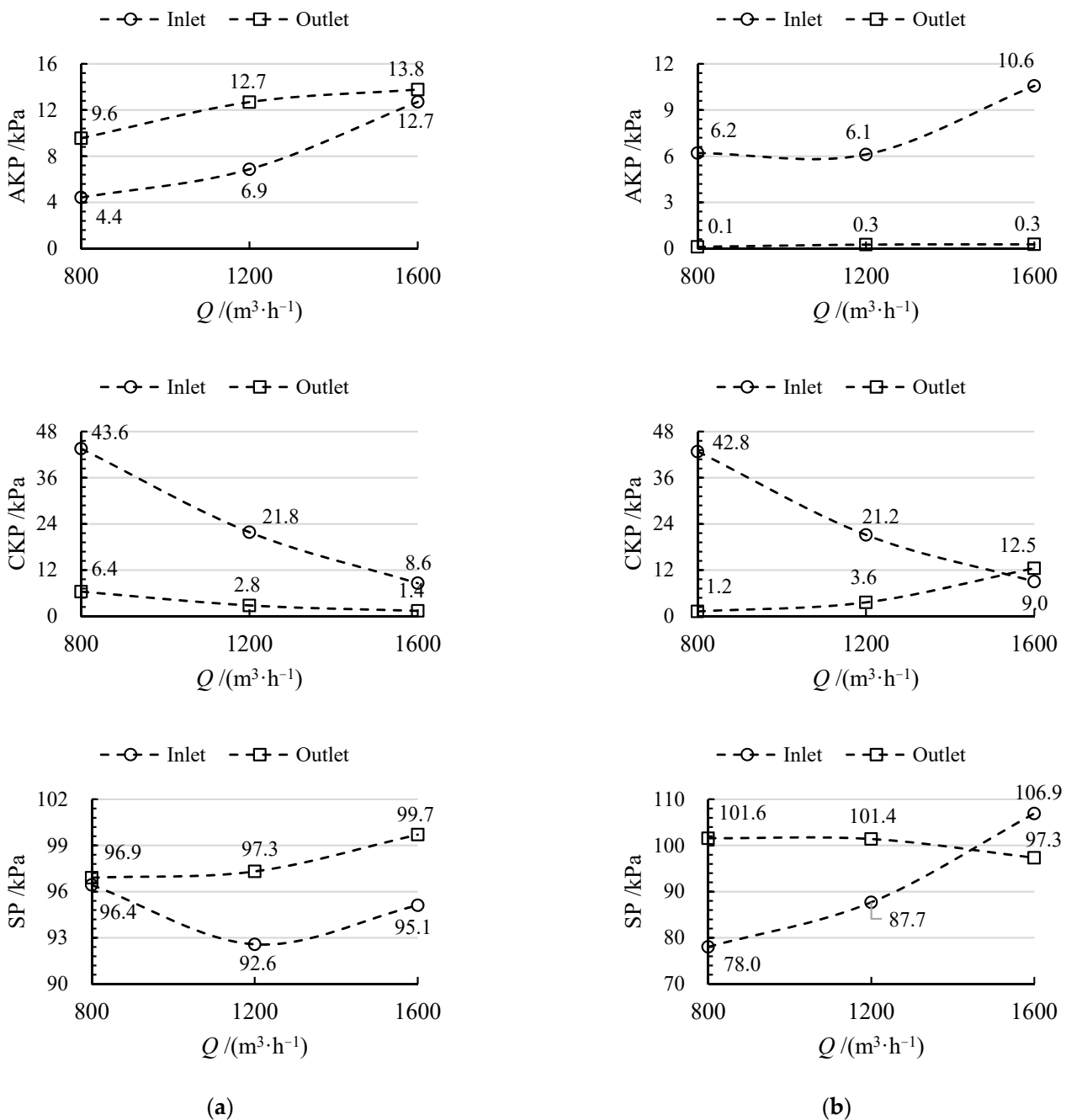


**Figure 12.** The distributions of kinetic pressure and static pressure on the inlet and outlet of the (a) guide vanes and (b) volute.

The radial coefficients of the guide vanes and the axial coefficients of the volute were defined as shown in Figure 13. To obtain the spatial distributions of energy losses during the energy conversion of the guide vanes, we studied the distributions of velocity and TEPR in three sections parallel to the outflow direction, as shown in Figure 14. When  $Q = 800 \text{ m}^3/\text{s}$ , the flow is unstable and large-scale vortex can be found inside the guide vanes. The high TEPR can be seen near trailing edge due to the flow separation under  $R^* = 0.2$  and  $0.9$ . There is a large vortex in the channel between the vanes under  $R^* = 0.55$ , which hinders the main flow and leads to a high TEPR. When  $Q = 1200 \text{ m}^3/\text{s}$ , the high TEPR can be found near the trailing edge and leading edge under  $R^* = 0.2$ , and the TEPR in the channel between the vanes is high under  $R^* = 0.55$ . When  $Q = 1600 \text{ m}^3/\text{s}$ , the flow field inside the guide vane is stable, and there is no obvious high TEPR. The distributions

of velocity and TEPR in three sections parallel to the outflow direction of the volute were shown in Figure 15. When  $Q = 800 \text{ m}^3/\text{s}$ , there is a large area of high TEPR near the inlet due to flow separation. The area of high TEPR is the largest under  $R^* = 0.55$ , and that is the smallest under  $R^* = 0.9$ . When  $Q = 1200 \text{ m}^3/\text{s}$ , the flow inside the volute is very stable and there is no evident high TEPR. When  $Q = 1600 \text{ m}^3/\text{s}$ , there is no evident flow separation near the inlet, but there is high TEPR near the outlet due to back flow. The area of high TEPR increases with the increase in  $R^*$ .

### 3.5. TEP Rate Distribution of Outlet Conduit

The recovering efficiency of kinetic energy in the pumping chamber determined the velocity distribution at the inlet of the outlet pipe. The inflow direction perpendicular to the inlet was defined as the positive direction of the normal velocity. The distributions of normal velocity on the inlet of two outlet pipes at different flow rates were obtained, as shown in Figure 16. Under  $Q = 800 \text{ m}^3/\text{s}$ , the normal velocity presents an axisymmetric distribution under the guide vanes scheme, and there is a large area of backflow near the wall of the outlet pipe. Compared with the guide vanes scheme, the distribution of normal velocity has no evident characteristics, but the distribution uniformity is higher, under the volute scheme. Under  $Q = 1200 \text{ m}^3/\text{s}$ , the distribution uniformity of normal velocity improves and there was no evident backflow under the two schemes. Under  $Q = 1600 \text{ m}^3/\text{s}$ , the normal velocity distribution uniformity under the guide vane scheme is further improved, but the normal velocity distribution uniformity under the volute scheme reduces and an evident reflux area can be found.

Figure 17 shows the distribution of TEPR in the outlet pipe between the guide vanes and volute scheme. The TEPR inside the outlet pipe decreases gradually with the flow direction both under the guide vanes and volute scheme, but the position of the high TEPR was closely related to the flow rates. Under  $Q = 800 \text{ m}^3/\text{s}$  and  $1200 \text{ m}^3/\text{s}$ , the TEPR near the inlet under the guide vanes scheme is higher than that under the volute scheme, owing to the fact that there is secondary flow near the inlet under the guide vanes scheme. Under  $Q = 1600 \text{ m}^3/\text{s}$ , the volute cannot effectively convert kinetic energy into pressure energy, resulting in a large area of backflow at the inlet of the outlet pipe. Therefore, the TEPR near the inlet under the volute scheme is higher than that under the guide vanes scheme.

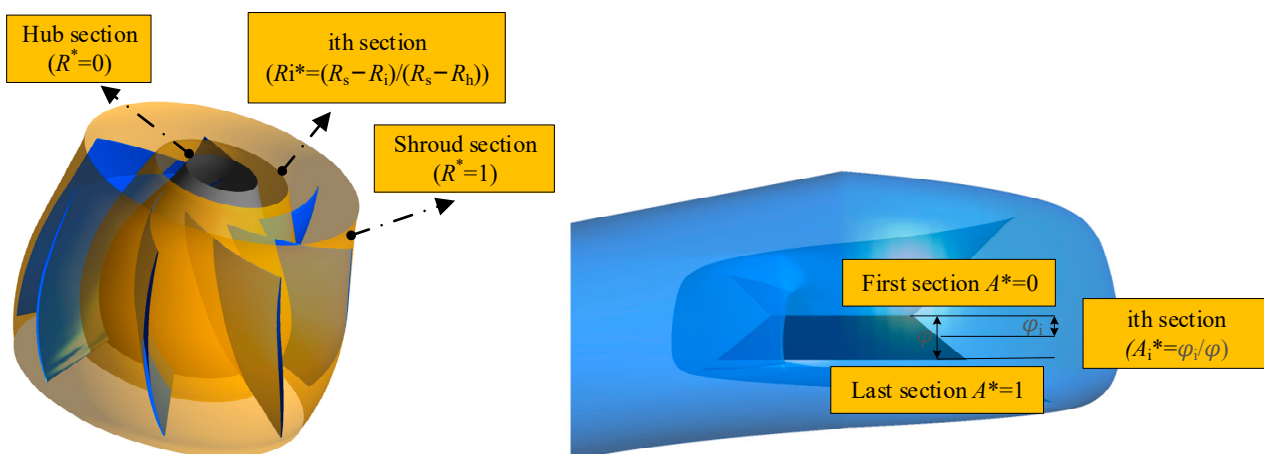
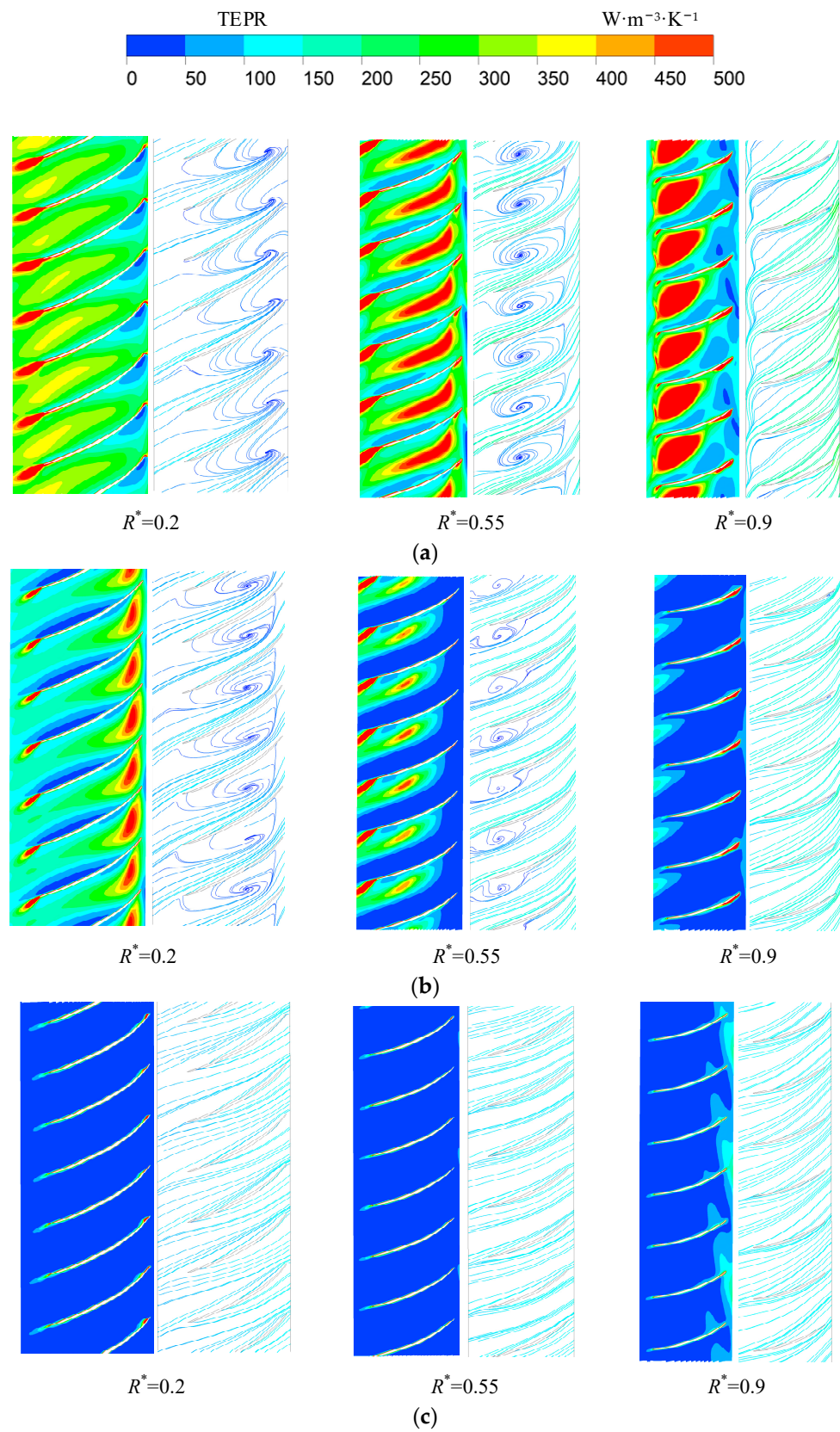
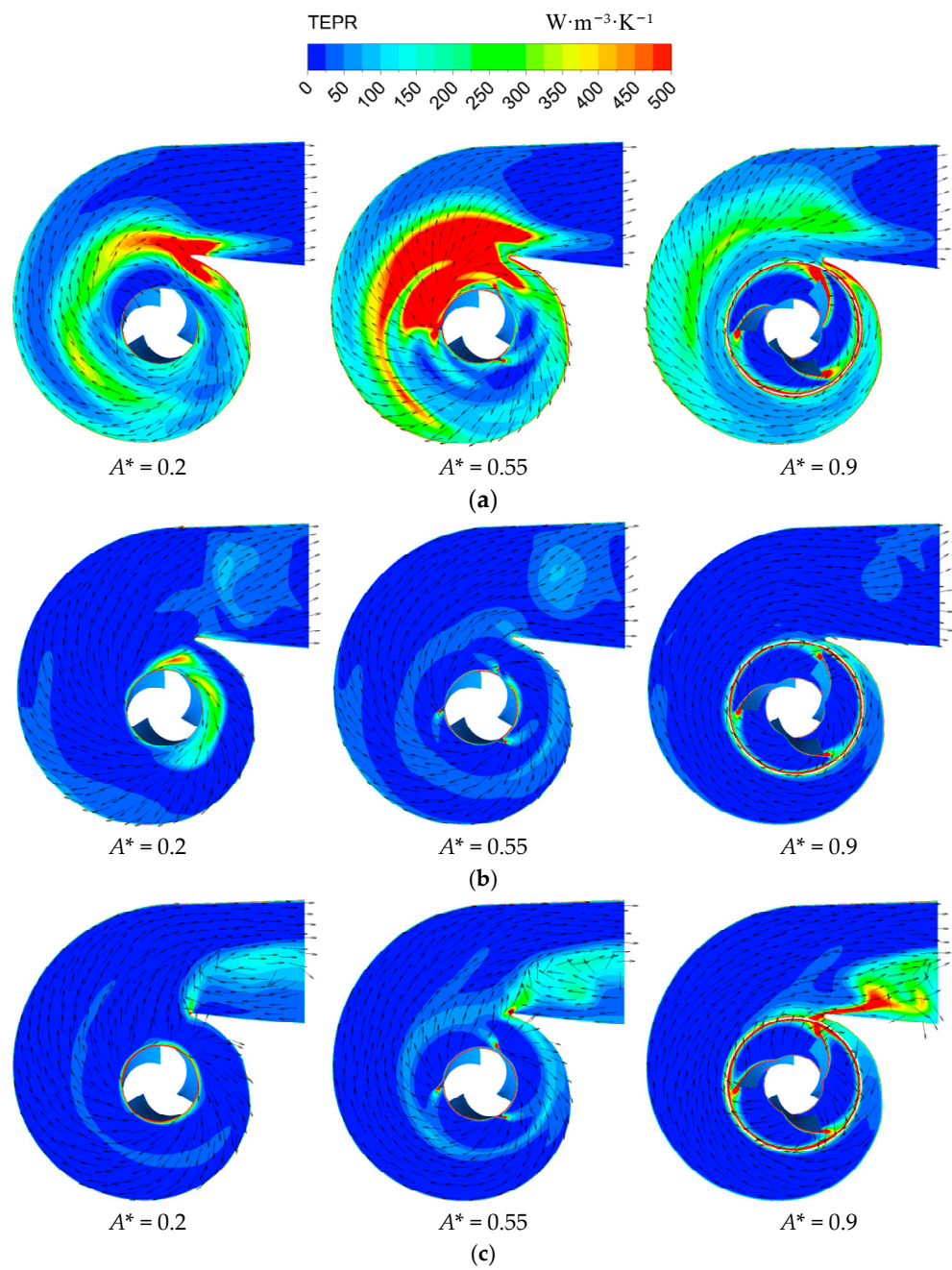


Figure 13. The axial sections of the impeller and pumping chamber.



**Figure 14.** The distribution of TEPR and velocity in the guide vanes at (a) 800 m<sup>3</sup>/h (b) 1200 m<sup>3</sup>/h and (c) 1600 m<sup>3</sup>/h.



**Figure 15.** The distribution of TEPR and velocity in the volute at (a)  $800 \text{ m}^3/\text{h}$  (b)  $1200 \text{ m}^3/\text{h}$  and (c)  $1600 \text{ m}^3/\text{h}$ .

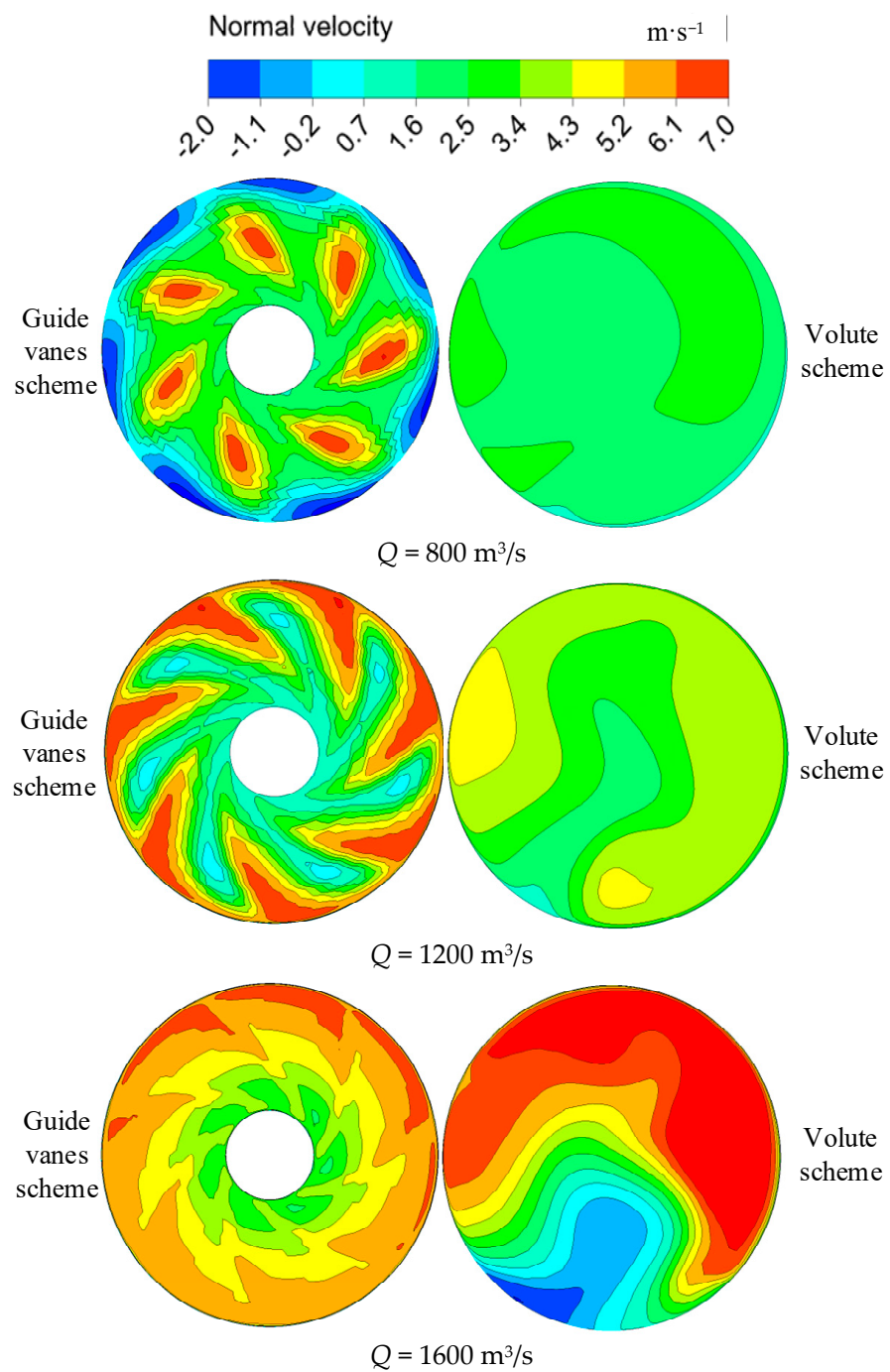


**Figure 16.** Distribution of normal velocity on the inlet of the outlet pipe at different flow rates.

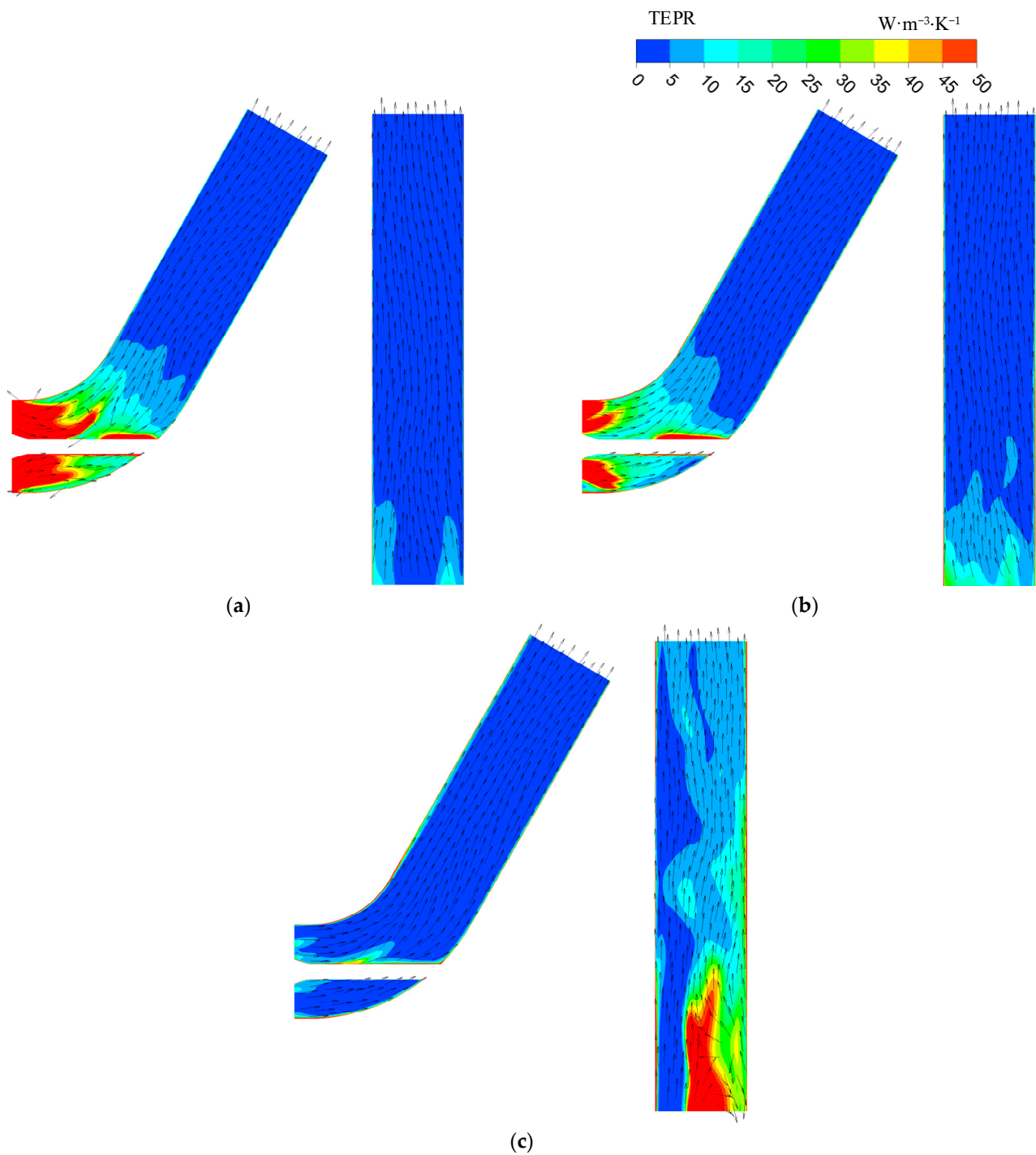


**Figure 17.** The distribution of TEPR and velocity in the section of the outlet pipe under the guide vanes and volute scheme at (a)  $800 \text{ m}^3/\text{s}$ , (b)  $1200 \text{ m}^3/\text{s}$  and (c)  $1600 \text{ m}^3/\text{s}$ .

#### 4. Conclusions

In this paper, the distribution of hydraulic losses during the recovery of rotating kinetic energy in two kinds of pumping chambers (guide vane and volute) of mixed-flow pumps were compared and analyzed using entropy production theory and CFD technology. The following conclusions were drawn:

(1) The efficiency and head under the volute scheme are higher than that under the guide vanes scheme, within  $Q = 800\text{--}1200 \text{ m}^3/\text{h}$ , but the efficiency and head under the volute scheme are lower than that under the guide vanes scheme, within  $Q = 1200\text{--}1600 \text{ m}^3/\text{h}$ .

(2) Compared with the RSI between impeller and volutes, the RSI between the impeller and guide vanes is stronger, which lead to high TEPR and velocity losses near the hub side of the impeller outlet, under small and design flow rates.

(3) Under small and design flow rates, the area of a high TEPR and the recovery efficiency of kinetic energy in the guide vanes are larger and lower than that in the volute, respectively, due to the serious flow separation near the suction side of the vanes. Under a large flow rate, the recovery efficiency of kinetic energy of the volute is lower than that of the guide vanes, caused by the backflow and high TEPR near the outlet of the volute.

(4) The area of a high TEPR caused by backflow in the outlet pipe under the guide vanes scheme is higher at 800m<sup>3</sup>/h and 1200 m<sup>3</sup>/h, but that under the volute scheme is higher under 1600 m<sup>3</sup>/h.

These results can provide a reference for the optimal design of mixed-flow pumps with a volute.

**Author Contributions:** Conceptualization: H.Z. and F.M.; methodology: H.Z. and F.M.; software: H.Z. and L.C.; validation: H.Z. and L.C.; formal analysis: H.Z. and L.C.; investigation: H.Z. and F.M.; resources: L.C.; data curation: L.C. and Y.L.; writing—original draft preparation: H.Z.; writing—review and editing: F.M. and X.W.; visualization: H.Z.; supervision: F.M.; project administration: Y.L.; funding acquisition: Y.L. All authors have read and agreed to the published version of the manuscript.

**Funding:** This research was funded by National Natural Science Foundation of China (51809120) and Industry-University-Research Collaboration of Jiangsu Province (BY2020373).

**Conflicts of Interest:** The authors declare no conflict of interest.

## Nomenclature

$H$ (m)	Pump head
$\eta$ (%)	Pump efficiency
$\rho$ (kg/m <sup>3</sup> )	Water density
$g$ (m/s <sup>2</sup> )	Gravitational acceleration
$p_{in}$ (Pa)	Total pressure of inlet
$p_{out}$ (Pa)	Total pressure of outlet
$P_s$ (W)	Shaft power
$Q$ (m <sup>3</sup> /h)	Volume flow rate
$Q_d$ (m <sup>3</sup> /h)	Best efficiency point
$H_d$	Pump head under best efficiency point
$u$ (m/s)	Velocity component in the $x$ direction of Cartesian coordinates
$v$ (m/s)	Velocity component in the $y$ direction of Cartesian coordinates
$w$ (m/s)	Velocity component in the $z$ direction of Cartesian coordinates
$div\left(\frac{\vec{q}}{T}\right)$ [W/(K·m <sup>3</sup> )]	Reversible heat transfer term
$\frac{\Phi}{T}$ [W/K·m <sup>3</sup> ]	Entropy production due to dissipation increase
$\frac{\Phi_q}{T^2}$ [W/(K·m <sup>3</sup> )]	Entropy production caused by the heat transfer
$s$ [J/(K·kg)]	Specific entropy
$\Phi_I$ (W/m <sup>3</sup> )	Indirect dissipation rate
$\Phi_D$ (W/m <sup>3</sup> )	Direct dissipation rate
$\Phi_T$ (W/m <sup>3</sup> )	Total dissipation rate
$S_{pro,I}$ (W/K)	Indirect entropy production
$S_{pro,D}$ (W/K)	Direct entropy production
$S_{pro,T}$ (W/K)	Total entropy production
$T$ (K)	Temperature
$\varepsilon$ (W/kg)	Dissipation rate of turbulent kinetic energy
$E_Q$	Measurement uncertainty of flow rate
$E_T$	Measurement uncertainty of shaft power
$E_H$	Measurement uncertainty of head
$E_S$	Measurement uncertainty of test bench

$\Gamma$ (m <sup>2</sup> /s)	Velocity circulation
$L$ (m)	Length of calculated ring
$v_u$ (m/s)	Absolute circumferential velocity
$r_c$ (m)	Calculated radius
$r_h$ (m)	Hub radius
$r_s$ (m)	Rim radius
$r^*$	Radial coefficient
$v_m$ (m/s)	Average axial velocity
$v_c$ (m/s)	Average circumferential velocity

### Abbreviation

CFD	Computational fluid dynamics
IEP	Indirect entropy production
DEP	Direct entropy production
TEP	Total entropy production
TEPR	Total entropy production rate
AKP	Axial kinetic pressure
CKP	Circumferential kinetic pressure
SP	Static pressure

### References

- Xingfan, G. *Modern Pump Theory and Design*; China Aerospace Publishing House: Beijing, China, 2011.
- Lianyuan, W.; Baoguo, L. Application of 500HW-7 typed volute mixed flow pump in sea salt production. *J. Salt Sci. Chem. Ind.* **2018**, *47*, 36–37.
- Zhu, H.; Bo, G.; Zhou, Y.; Rentian, Z.; Jilin, C. Performance prediction of pump and pumping system based on combination of numerical simulation and non-full passage model test. *J. Braz. Soc. Mech. Sci. Eng.* **2019**, *41*, 1–12. [[CrossRef](#)]
- Yousefi, H.; Noorollahi, Y.; Tahani, M.; Roshanak, F.; Salman, S. Numerical simulation for obtaining optimal impeller's blade parameters of a centrifugal pump for high-viscosity fluid pumping. *Sustain. Energy Technol. Assess.* **2019**, *34*, 16–26. [[CrossRef](#)]
- Zhang, W.; Shi, L.; Tang, F.; Xiaohui, D.; Haiyu, L.; Zhuangzhuang, S. Analysis of inlet flow passage conditions and their influence on the performance of an axial-flow pump. *Proc. Inst. Mech. Eng. Part A J. Power Energy* **2021**, *235*, 733–746. [[CrossRef](#)]
- Liu, Y.; Tan, L. Tip clearance on pressure fluctuation intensity and vortex characteristic of a mixed flow pump as turbine at pump mode. *Renew. Energy* **2018**, *129*, 606–615. [[CrossRef](#)]
- Han, Y.; Tan, L. Influence of rotating speed on tip leakage vortex in a mixed flow pump as turbine at pump mode. *Renew. Energy* **2020**, *162*, 144–150. [[CrossRef](#)]
- Li, W.; Zhang, Y.; Shi, W.; Dazhuan, W. Numerical simulation of transient flow field in a mixed-flow pump during starting period. *Int. J. Numer. Methods Heat Fluid Flow* **2018**, *29*, 1319–1322. [[CrossRef](#)]
- Xu, Y.; Tan, L.; Liu, Y.; Shuliang, C. Pressure fluctuation and flow pattern of a mixed-flow pump under design and off-design conditions. *Proc. Inst. Mech. Eng. Part C J. Mech. Eng. Sci.* **2018**, *232*, 2430–2440. [[CrossRef](#)]
- Ji, L.; Li, W.; Shi, W.; Fei, T.; Shuo, L.; Ramesh, A. Influence of different blade numbers on the performance of “saddle zone” in a mixed flow pump. *Proc. Inst. Mech. Eng. Part A J. Power Energy* **2021**, *15*, 09576509211046074. [[CrossRef](#)]
- Kim, S.; Kim, Y.I.; Kim, J.H.; Choi, Y.-S. Design optimization for mixed-flow pump impeller by improved suction performance and efficiency with variables of specific speeds. *J. Mech. Sci. Technol.* **2020**, *34*, 2377–2389. [[CrossRef](#)]
- Kim, S.; Kim, Y.I.; Kim, J.H.; Young-Seok, C. Three-objective optimization of a mixed-flow pump impeller for improved suction performance and efficiency. *Adv. Mech. Eng.* **2019**, *11*, 1687814019898969. [[CrossRef](#)]
- Bejan, A. *Entropy Generation through Heat and Fluid Flow*; Wiley: Hoboken, NJ, USA, 1982.
- Spurk, J.H. *Fluid Mechanics*; Springer: Berlin/Heidelberg, Germany, 1994.
- Herwig, H.; Kock, F. Direct and indirect methods of calculating entropy generation rates in turbulent convective heat transfer problems. *Heat Mass Transf.* **2007**, *43*, 207–215. [[CrossRef](#)]
- Herwig, H.; Kock, F. Local entropy production in turbulent shear flows: A tool for evaluating heat transfer performance. *J. Therm. Sci.* **2006**, *15*, 159–167. [[CrossRef](#)]
- Kock, F.; Herwig, H. Local entropy production in turbulent shear flows: A high-Reynolds number model with wall functions. *Int. J. Heat Mass Transf.* **2004**, *47*, 2205–2215. [[CrossRef](#)]
- Kock, F.; Herwig, H. Entropy production calculation for turbulent shear flows and their implementation in cfd codes. *Int. J. Heat Fluid Flow* **2005**, *26*, 672–680. [[CrossRef](#)]
- Hou, H.; Zhang, Y.; Zhou, X.; Haiseng, H. Optimal hydraulic design of an ultra-low specific speed centrifugal pump based on the local entropy production theory. *Proc. Inst. Mech. Eng. Part A J. Power Energy* **2019**, *233*, 715–726. [[CrossRef](#)]

20. Guan, H.; Jiang, W.; Yang, J.; Yuchuan, W.; Xinghai, Z.; Junxue, W. Energy loss analysis of the double-suction centrifugal pump under different flow rates based on entropy production theory. *Proc. Inst. Mech. Eng. Part C J. Mech. Eng. Sci.* **2020**, *234*, 4009–4023. [[CrossRef](#)]
21. Yang, F.; Li, Z.; Hu, W.; Chao, L.; Dongjin, J.; Dongsheng, L.; Ahmed, N. Analysis of flow loss characteristics of slanted axial-flow pump device based on entropy production theory. *R. Soc. Open Sci.* **2022**, *9*, 211208. [[CrossRef](#)] [[PubMed](#)]